Elemental segregation to lattice defects in the CrMnFeCoNi high-entropy alloy during high temperature exposures

Milan Heczko[a,b,1,2], Veronika Mazánová[a,b,2], Roman Gröger[a], Tomáš Záležák[a], Mohammad S. Hooshmand[c], Easo P. George[d,e], Michael J. Mills[b], Antonín Dlouhý[a]

[a] *Institute of Physics of Materials and CEITEC IPM, Czech Academy of Sciences, Žižkova 22, 616 00 Brno, Czech Republic*
[b] *Center for Electron Microscopy and Analysis, Department of Materials Science and Engineering, The Ohio State University, 1305 Kinnear Rd, Columbus, OH 43212, USA*
[c] *Department of Materials Science and Engineering, University of California, 2607 Hearst Ave, Berkeley, CA 94720, USA*
[d] *Materials Science and Technology Division, Oak Ridge National Laboratory, Oak Ridge, TN 37831, USA*
[e] *Materials Science and Engineering Department, University of Tennessee, Knoxville, TN 37996, USA*

ABSTRACT

The influence of small plastic pre-strains on the elevated-temperature stability and microstructure of the equiatomic CrMnFeCoNi FCC solid solution is investigated. Particular attention is given to whether any of the alloy elements segregate to individual dislocations. To that end, CrMnFeCoNi samples were first deformed in tension at room temperature to plastic strains of 0.2 and 2.3%, and subsequently annealed at 973 K for 800 hours. The pre-strains activated planar slip of 1/2<110>-type dislocations on {111}-type glide planes. Interactions of this planar slip with special Σ3 grain boundaries formed a large number of dislocation segments with a <110>-type crystallographic orientation suitable for a credible end-on analysis of dislocation cores in HR-STEM. The cores of the 1/2<110> dislocations pushed up against the investigated grain boundaries were found to be close to the compact configuration. Within the sensitivity of the Super-X EDS mapping, no concentration gradient was detected near dislocations that would indicate enrichment at dislocation cores of any of the elemental constituents of the alloy after the pre-deformation and annealing. However, a Cr-rich tetragonal sigma phase nucleated and grew at grain boundary triple junctions during this anneal, processes that were not accelerated by the enhanced dislocation density present after pre-strain. A clear chromium gradient was

[1] *Corresponding author, Email address: heczko.2@osu.edu*
[2] *Present address: The Ohio State University, Department of Materials Science and Engineering, Center for Electron Microscopy and Analysis (CEMAS), 1305 Kinnear Rd, Suite 100, Columbus, OH 43212, USA*

observed in the Cr-depleted zones near grain boundaries suggesting that Cr transport occurred by relatively slow diffusion from the bulk to the grain boundaries and then by relatively fast diffusion along the grain boundaries to the precipitates. Accompanying the Cr depletion near grain boundaries is a simultaneous Ni and Mn enrichment, which promotes formation of the $L1_0$ NiMn phase that is observed on the grain boundaries after prolonged annealing.

KEYWORDS:

High entropy alloys, CrMnFeCoNi Cantor alloy, thermodynamic stability, dislocation cores, elemental segregation, sigma phase

1. INTRODUCTION

The strength of high-temperature materials generally stems from two- or multi-phase microstructures in which the matrix phase is a complex solid solution containing many elements, see e.g. [1,2]. In modern nickel-base superalloys, Ni-rich matrices dissolve considerable amounts of Cr and Co [3], while Cr is also an important solute in the Fe-rich matrices of high-Cr steels [4]. It is thus not surprising that the mechanical properties of recently developed multi-principal element alloys (MPEA), including the single-phase CrMnFeCoNi alloy with the face-centered cubic (FCC) structure [5–7], and its quaternary, ternary and binary equiatomic subsets [6,8], receive increasing attention. These alloys are model surrogates for complex, off-equiatomic, solid solutions in multiphase superalloys [9]. Alloys in which all elements are present in equiatomic proportions, and thus none of them qualifies as a solute and/or solvent, may serve as a starting point to study complex interactions between individual chemical species and lattice defects during high temperature exposures. Understanding the interactions in the equiatomic solid solutions may, in turn, help shed light on processes which govern mechanical responses of off-equiatomic matrices in engineering alloys.

Due to their high configurational entropy, quinary and higher order equiatomic solid solutions were expected to possess improved thermodynamic stability and remain in the solid solution state, particularly at high temperatures where the entropy term dominates the Gibbs free energy [10]. However, several studies have now demonstrated that even the Cantor alloy (CrMnFeCoNi), which was once thought to be the exemplar of a stable solid solution, decomposes into a multiphase state at elevated temperatures in the range 723 - 973 K (0.47 - 0.63 T_m, where T_m = 1553 K is the solidus temperature [6,8]), see e.g. [11–

13]. These and later studies reported two important results that are relevant to the objectives of the present work. First, chromium readily forms a Cr-rich sigma phase [11] and, second, the sigma precipitates were almost exclusively found on grain boundaries suggesting that planar defects are required as sites for heterogeneous nucleation [13]. Some evidence has recently also been provided for the nucleation of the sigma phase on dislocations in a heavily deformed CrMnFeCoNi alloy [14]. Zhou et al. [14] combined cold-rolling with either annealing at 873 K for 10 min to obtain partial recovery or annealing at 973 K for 40 minutes to reach a fully recrystallized state. They observed nucleation of spherical nano-sized Cr-rich precipitates either at the dislocation cell walls after partial recovery or at the dislocations in the interiors of grains after recrystallization.

Notwithstanding these limited results, the role of dislocations in the decomposition process needs further exploration. Although dislocation cores represent paths of high diffusivity, it remains unclear whether (and to what extent) they serve as effective channels for chromium transport to grain boundaries, where the Cr-rich sigma phase nucleates and grows. If in fact they are effective in transporting chromium, it stands to reason that chromium should be enriched in the dislocation core regions.

Additionally, if there is segregation of chromium to dislocation cores, it may fundamentally alter the motion of dislocations during high temperature deformation. In this context, Kang et al. investigated creep behavior of the CrMnFeCoNi alloy in the temperature range 800 - 923 K (0.52 - 0.59 T_m) [15]. They reported a change in the Norton stress exponent from 5.8 (at low stresses up to 40 MPa) to 3.1 (at high stresses above 40 MPa) which may suggest a transition from metal- to alloy-type creep behavior with increasing applied stress. Without any microstructural evidence, Kang et al. attributed this macroscopic effect to segregation of Cr atoms to dislocations and the corresponding viscous glide of dislocations at high applied stresses [15].

In view of these open questions, the present study sets out to answer the fundamental question: does segregation of Cr atoms to dislocations occur in the quinary equiatomic alloy CrMnFeCoNi? To that end, samples of the alloy were pre-deformed in tension at room temperature up to plastic strains of ~2% followed by annealing of the pre-strained material at 973 K (0.62 T_m) for 800 hours. The selected temperature and annealing time fall in the range in which precipitation of the Cr-rich sigma phase has been reported and which is also typical for CrMnFeCoNi creep studies [16]. We use advanced electron microscopy methods to characterize the 1/2<110>-type dislocations with particular attention given to the core structure and its chemical composition.

2. EXPERIMENTAL

An equiatomic quinary CrMnFeCoNi was arc melted and drop cast into a copper mold. The drop-cast ingots were homogenized, cold rolled and subsequently subjected to a recrystallization treatment at 1173 K for 1 hour to obtain single-phase FCC microstructure. These procedures are similar to those described in detail in an earlier paper [7]. Flat dog-bone-shaped tensile specimens with a gauge length of 25 mm were machined from the recrystallized sheets by electric discharge machining (EDM) with their longitudinal axes parallel to the rolling direction of the sheet. The specimens were ground on each side using 2000 grit SiC paper, resulting in a final specimen thickness of 3.2 mm and a gauge section width of 4 mm.

The average grain size (d) was estimated using Heyn´s linear intercept method (ASTM E112) with seven horizontal and seven vertical lines for each micrograph. Three scanning electron microscope (SEM) micrographs collected using the back-scattered electron (BSE) imaging mode were analyzed for each state of material. Additionally, the average crystallite size (c) was estimated, which included also the twin boundaries in the linear intercept method [17]. The results are summarized in **Table 1**.

Two specimens were pre-deformed in tension at a constant crosshead displacement rate (initial engineering strain rate 1×10^{-3} s^{-1}) using a computer controlled electro-hydraulic MTS 809 testing machine. The machine was equipped with hydraulic grips and axial extensometer with a 12 mm base. Tests were interrupted at plastic strain levels of either 0.2 or 2.3%; the corresponding stress-strain curves are presented in **Fig. 1**.

Even though the primary focus of the present study is the possible segregation of individual atomic species to lattice defects at elevated temperature, the pre-deformation experiments were carried out at room temperature (RT). We did this because, in the CrMnFeCoNi alloy, the early stages of RT plasticity are associated with planar dislocation slip on {111}-type crystallographic planes [7]. These planar dislocation structures interact with special boundaries, like coherent Σ3 annealing twin or Σ11 tilt boundaries, such that a leading dislocation segment pushed against the boundary is often aligned parallel to a <110>-type crystallographic direction. This specific alignment results from the orientation of Σ3 and Σ11 boundaries which are parallel to {111}- and {311}-type crystallographic planes, respectively. The <110> end-on orientation of dislocation lines facilitates subsequent analysis of their cores in the high-resolution scanning transmission electron microscopy (HR-STEM) mode. A similar technique was first proposed and applied by Smith et al. [18].

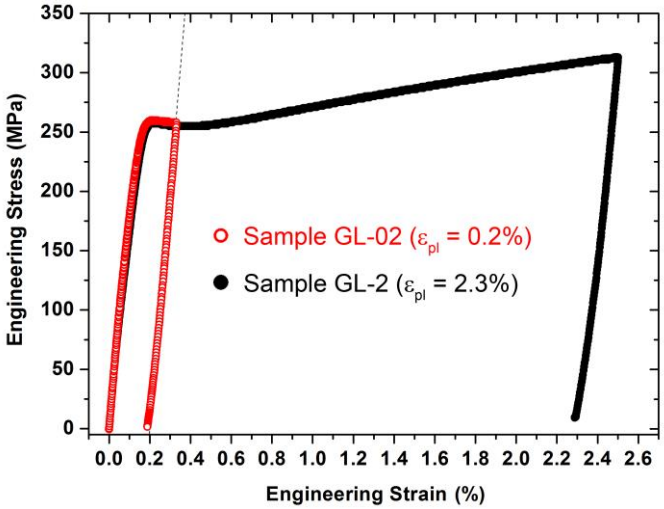

Figure 1: *Tensile stress-strain curves of the CrMnFeCoNi alloy pre-deformed at room temperature to engineering plastic strains of 0.2% (sample GL-02) and 2.3% (sample GL-2).*

After pre-straining at RT, the dog-bone specimens were cut in half. Each half consisted of one specimen head and part of the gauge length. The microstructures of one head and its associated gauge length were investigated directly after the pre-deformation using SEM and transmission electron microscopy (TEM). In **Table 1**, these material states are referred to as H and GL-x, where x is either 02 or 2 depending on the amount of plastic strain (0.2% and 2.3%) accumulated during the pre-deformation. The second half of each pre-strained sample was annealed at T_a = 973 K (0.63 T_m) for t_a = 800 hours, yielding the material states H-A and GL-x-A listed in **Table 1**. The annealing treatment was performed in a resistance furnace under a protective atmosphere of argon keeping the annealing temperature variations within ±1 K range.

Table 1: *Investigated material states, their deformation and microstructural characteristics.*

Material state	E (GPa)	$\sigma_{0.2}$ (MPa)	ε_{pl} (%)	ε_{tot} (%)	T_a (K)	t_a (h)	d (µm)	c (µm)	ρ_D (10^{13} m^{-2})	A_σ (%)
H	-	-	-	-	-	-	18.8 ± 5.7	9.5 ± 0.6	~ 5 × 10^{-1}	
H-A	-	-	-	-	973	800	19.2 ± 1.2	10.5 ± 1.6	~ 5 × 10^{-1}	1.4±0.1
GL-02	203	260	0.2	0.3	-	-			4.8 ± 1.5	
GL-02-A	203	260	0.2	0.3	973	800			-	
GL-2	198	255	2.3	2.5	-	-	19.5 ± 5.9	8.8 ± 2.7	9.4 ± 2.8	
GL-2-A	198	255	2.3	2.5	973	800	18.9 ± 1.0	10.0 ± 0.8	7.2 ± 2.5	1.5±0.1

H - specimen head, GL - specimen gauge length, E - Young's modulus, $\sigma_{0.2}$ - 0.2% offset yield strength, ε_{pl} - plastic strain, ε_{tot} - total strain, T_a - annealing temperature, t_a - annealing time, d - grain size, c - crystallite size, ρ_D - dislocation density, A_σ - sigma phase area fraction

Thin plates for microstructural investigations were cut parallel to the tensile axis of the pre-strained samples using an EDM. The plates were ground on SiC papers down to a thickness of 0.15 mm before discs 3 mm in diameter were punched out. The discs were electropolished in a twin jet polishing system TenuPol5 filled with electrolyte containing 95% acetic acid and 5% perchloric acid (by volume). The optimum polishing conditions were obtained at 80-90 V, 0.2 mA and temperature between 12-16 °C. Further details on the preparation of the TEM samples can be found elsewhere [13]. The microstructure was analyzed at several length scales, first using the dual-beam SEM Tescan LYRA 3 XMU FEG equipped with the electron back-scatter diffraction (EBSD) detector from Oxford Instruments and controlled by the Oxford AZtec software. High resolution EBSD maps were collected at an accelerating voltage of 20 keV using a spot size of 60 nm. Additionally, the SEM FEI Helios 660 Nanolab from Thermo Fisher Scientific (TFS) operating at 10 keV and working distance of 6 mm was employed to collect images in the BSE imaging mode. Ten images of 100×75 μm in size were acquired for each material state to characterize grain size and the area fraction of the Cr-rich sigma phase using the image analysis software ImageJ.

Characterization of grain boundaries, dislocation structure and phase composition at length scales down to nanometers was performed by scanning transmission electron microscopy (STEM) using the JEOL JEM-2100F S/TEM operating at 200 kV and equipped with X-Max80 energy dispersive X-ray spectroscopy (EDS) detector from Oxford Instruments. We have combined tilting experiments, stereo pair, convergent beam electron diffraction (CBED) and cube projection techniques in order to evaluate dislocation Burgers vectors, STEM foil thickness and describe the crystallography and spatial distribution of defects [19–22]. Dislocation densities were estimated by means of a statistical method elaborated by Ham [23]. STEM foils tilted into specific low index crystallographic zones of the <110>-type were investigated in a high-angle annular dark-field (HAADF) regime in an image-corrected and monochromated TFS/FEI Titan-Themis 60-300 kV S/TEM. The corresponding atomic resolution images together with the high spatial resolution chemical data from a Super-X EDS detector provided detailed information on the atomic structure and chemical composition of the dislocation cores. The data were collected and processed using the TFS Velox software. In particular, the raw data in the original spectral maps were quantified using standard Cliff-Lorimer (K-factor) fit (default k-factors available in Velox were used as well as the Brown-Powell empirical ionization cross-section model), including absorption correction and background subtraction. The atomic resolution STEM images were corrected for possible drift and scanning beam distortions using the drift corrected frame integration (DCFI) function of Velox.

Maps of dislocation cores were generated by the center of symmetry (COS) and the Nye tensor techniques [24]. The COS analysis, detailed in Vorontsov et al. [25], determines the degree of centro-symmetry for each atomic column in the experimental HAADF-STEM image and thus identifies faults in the stacking sequence. Centroids of the atomic columns are determined by cross correlating the images with Gaussian peaks with well-defined maxima. All stages of the processing sequence are performed using MATLAB® with the Image Processing Toolbox [18,25]. The Nye tensor component distributions are computed by a modification of the method proposed by Hartley and Mishin [24] for 3D crystals that made it applicable to 2D HAADF-STEM images. The 3D lattice is projected onto the plane of view, perpendicular to the electron beam and the dislocation line. The projected lattice is treated as a 2D lattice with newly defined nearest neighbor vectors. Note that the 2D Nye analysis does not provide any information about the screw component of the Burgers vector due to a lack of displacement data parallel to the dislocation line. The ability of the COS to detect the entire stacking fault is complementary to the Nye tensor analysis which, on the other hand, provides better information on the positions of the Shockley partials [18].

3. RESULTS

3.1 SEM

High EBSD signal to noise ratios, and thus EBSD maps of high quality, were obtained when the thin disc foils 3 mm in diameter were inspected in SEM after the electropolishing. During the EBSD analysis, the discs were placed into a special TEM disc foil holder. The EBSD maps were collected from all six material states listed in **Table 1**. In **Fig. 2** we compare results obtained for the initial state of the CrMnFeCoNi alloy after recrystallization (material state H, **Fig. 2a**) and after subsequent pre-deformation to 2.3% plastic strain (material state GL-2, **Fig. 2b**). Results presented in **Fig. 2** suggest that the microstructure is not significantly altered by the mild pre-strain of the order of 2%.

Next we looked for changes in the microstructure of all deformed and undeformed material states after annealing at 973 K for 800 hours. Representative results are presented in **Fig. 3** which shows the EBSD grain orientation maps and image quality maps for the annealed material states H-A (**Figs. 3a** and **3b**) and GL-2-A (**Figs. 3c** and **3d**). Quantitative analyses of the image quality maps yielded grain sizes of 19.2±1.2 μm and 18.9±1.0 μm for the material states H-A and GL-2-A, respectively. These data are summarized in **Table 1** together with grain sizes evaluated for the material states H and GL-2 prior to annealing. In addition, the distributions of grain boundary misorientation angles were plotted using the EBSD map data of H-A (**Fig. 3a**) and GL-2-A (**Fig. 3c**) material states. These distributions are shown in **Fig. S1** in Supplementary Material. Comparing all the values and considering

the indicated experimental scatter, it can be concluded that neither the pre-deformation to 2.3% tensile plastic strain nor the annealing at 973 K for 800 hours resulted in significant variations of the grain size as compared to the initial microstructure after recrystallization. Dark regions in the image quality maps shown in **Figs. 3b** and **3d** were identified as the tetragonal Cr-rich sigma phase, (ICSD structure file no. 102747, tetragonal P42mnm, lattice parameters a = 0.87966 nm, c = 0.45582 nm [26]). The sigma phase particles nucleate and grow exclusively at grain boundaries with a high preference for their triple points. The distribution plots in **Fig. S1** demonstrate that sigma phase nucleation is associated preferentially with the high angle grain boundaries (HAGBs). Only 17.5% and 22.2% of special coherent twin boundaries form triple junctions which host the sigma phase particles in the material states H-A and GL-2-A, respectively. The corresponding sigma phase area fractions were obtained from image analysis (as percentages of the total investigated area): 1.4±0.1 % and 1.5±0.1 % for the material states H-A and GL-2-A, respectively, see **Table 1**. Similar to the results of the grain size measurements, the differences in the sigma phase area fractions are within the experimental error and thus we can conclude that the pre-deformation, which preceded the annealing step, had no significant influence on the sigma phase precipitation. Further work, involving the acquisition of high resolution EBSD maps, revealed that no sigma phase particles were present inside grains. Taking into account our working SEM beam size of 60 nm and the size of the intragranular sigma particles reported by Zhou et al. [14], there was a reasonable chance of detection if such particles existed in our material state GL-2-A.

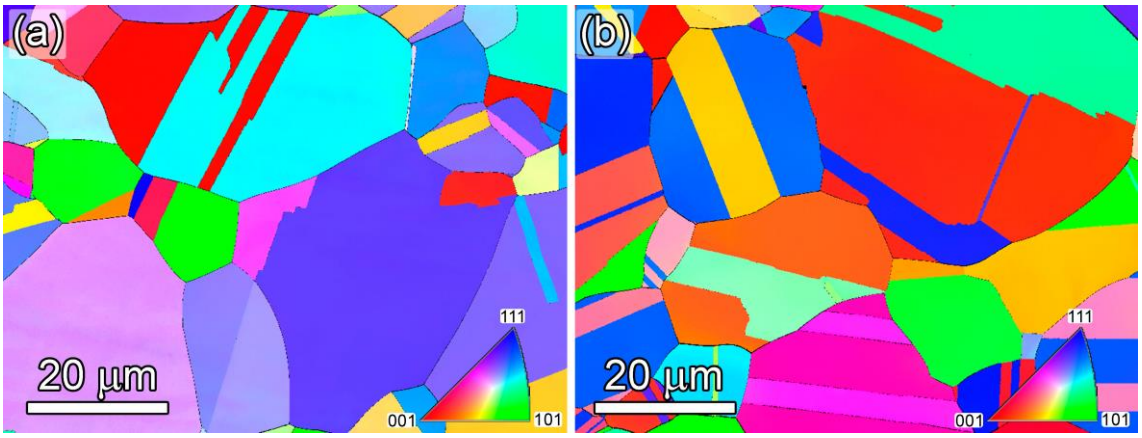

Figure 2: *EBSD maps which render crystallographic directions perpendicular to the plane of the figure, see the color coding in the inset. (a) initial state of the CrMnFeCoNi alloy after recrystallization (material state H). (b) after pre-straining to tensile plastic strain of 2.3% (material state GL-2).*

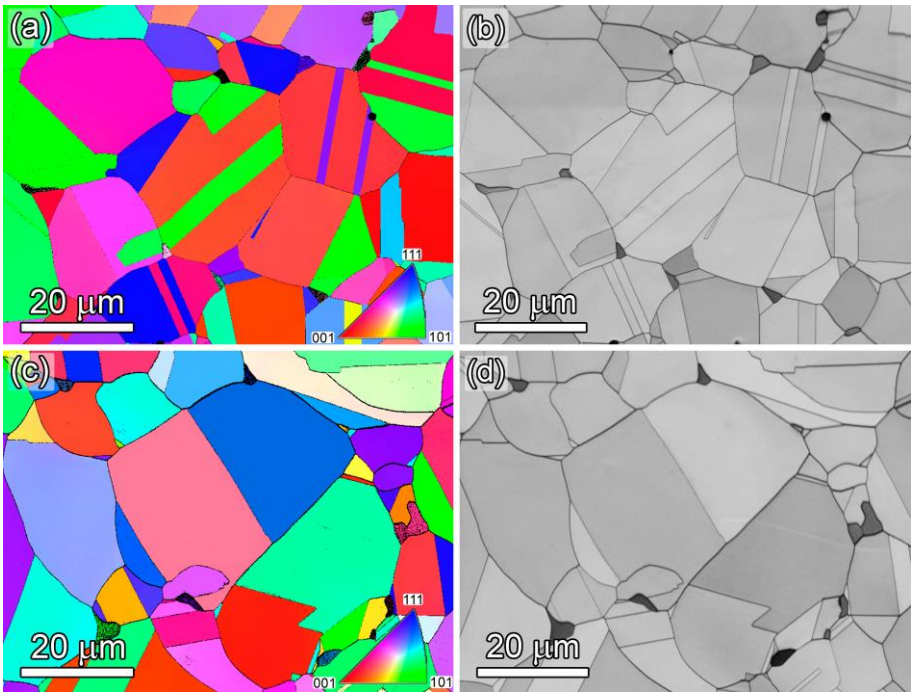

Figure 3: *EBSD maps (left) which render crystallographic directions perpendicular to the plane of the figure (see the color coding in the inset), and the corresponding image quality maps (right). (a and b) un-deformed head of the sample after annealing at 973 K for 800 hours (material state H-A). (c and d) sample gauge length after plastic strain of 2.3% followed by annealing at 973 K for 800 hours (material state GL-2-A). The dark regions in images (b) and (d) were identified as the tetragonal Cr-rich sigma phase.*

3.2 STEM

3.2.1 Interactions of 1/2<110>-type dislocations with special boundaries

As was explained in the experimental section, dislocation segments whose line orientations are parallel to low index crystallographic directions are required for efficient analysis of the atomic structure and chemical composition of dislocation cores. **Figure 4** illustrates one example of how such stable dislocation line orientations are established in the investigated CrMnFeCoNi alloy after pre-deformation to 0.2% plastic strain at RT. In **Fig. 4a**, planar slip on the $(1\bar{1}\bar{1})$ octahedral plane piles up dislocations against a (311) grain boundary plane. The head (leading) dislocation of the pile-up is oriented along the $\xi_{GB} = [01\bar{1}]$ crystallographic direction which is common to both, the slip and the boundary planes. A complete set of the grain boundary parameters is summarized in **Table S1** of the Supplementary Material. Several two beam conditions with different operating diffraction

vectors **g** were established in tilting experiments in order to evaluate Burgers vector **b** of the dislocations in the pile-up using the simple invisibility criterion **g**·**b** = 0 [19]. These experiments yielded **b** = ±1/2[$01\bar{1}$]. Therefore, the head dislocation of the pile up which is pushed against the (311) boundary has a screw character. An anaglyph shown in **Fig. 4b** enables viewing of the spatial arrangement of the boundary plane and gliding dislocations and, in combination with the cube projection method [21], facilitates crystallographic analysis.

Red-cyan type 3D glasses are required for 3D perception of the microstructure shown in **Fig. 4b**. Similar stable <110> orientations of dislocation segments can be produced by piling dislocations up against the Σ3 coherent twin boundaries as reported by Smith et al. [18]. In what follows, we select these specific dislocation line orientations for HR-STEM analysis of their cores.

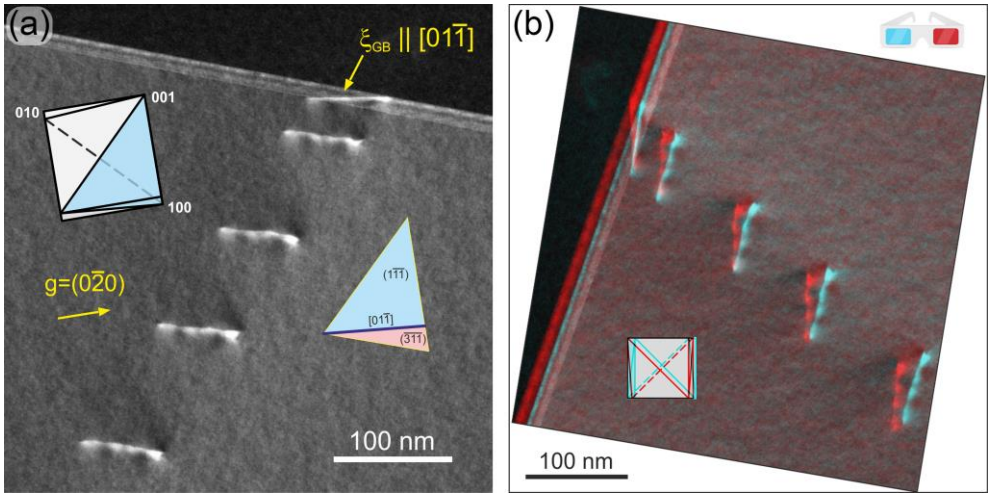

Figure 4: *(a) HAADF-STEM image shows planar dislocation slip in the* $(1\bar{1}\bar{1})$ *octahedral plane (blue) after 0.2 % tensile plastic strain in the CrMnFeCoNi alloy at RT (material state GL-02). Dislocations pile up against a* (311) *grain boundary plane (pink). The screw dislocation at the head of the pile-up is oriented parallel to the common* ξ_{GB} = [$01\bar{1}$] *crystallographic direction. (b) Anaglyph of the HAADF-STEM stereopair which allows a 3D perception of the dislocation-boundary arrangement and facilitates the crystallographic analysis, see text for further details.*

3.2.2 Analysis of dislocation cores

High resolution STEM was used to provide information on possible segregation of elements to grain boundaries and <110>-oriented dislocations. As confirmed earlier for the

CrMnFeCoNi alloy [7,18], the dislocation line segments with the <110> crystallographic orientation exhibit either 60° or pure screw character, depending on the 1/2<110>-type Burgers vectors, making them ideal configurations for atomic resolution microscopy [18]. Several sites containing dislocation pileups at Σ3 coherent twin boundaries were inspected and analyzed in the material state GL-2. One example shown in **Fig. 5a** presents a low angle annular dark field (LAADF) STEM image of a Σ3 coherent twin boundary and the nearby dislocation structure. Crystallographic orientation of the boundary was determined and the $(111)_T$ slip plane oriented edge-on was found in the annealing twin. The letter X and a black rectangle mark a region with an end-on oriented dislocation (lower left corner of **Fig. 5a**) which is shown in detail in the corresponding FFT filtered high resolution HAADF-STEM images in **Figs. 5b** and **5c**. This dislocation represents the first dislocation of a pile-up (not recorded in **Fig. 5a**) impinging on the annealing twin boundary.

Based on the experimental data of **Fig. 5**, the positions of both the twinning plane $(11\bar{1})_{M/T}$ and the core of the dislocation are highlighted in the COS map of local lattice distortions in **Fig. 6a**. The Nye tensor analysis based on the same experimental intensities, was also performed to identify expected positions of partial dislocations. Corresponding distribution maps of α_{31} and α_{32} Nye tensor components are plotted in **Figs. 6b** and **6c**, respectively.

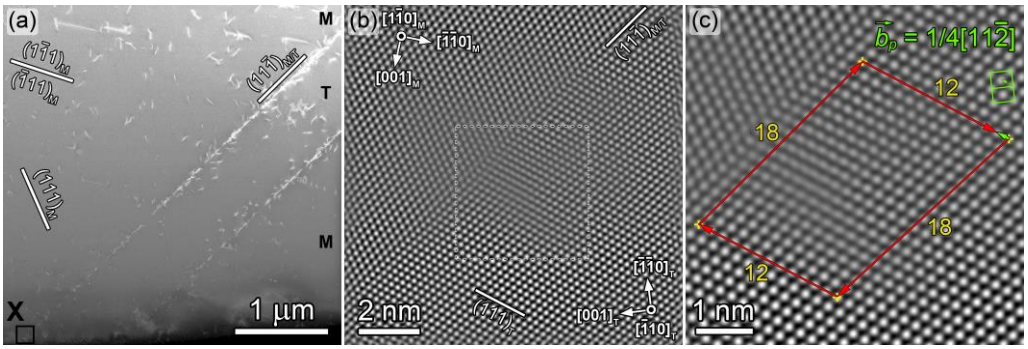

Figure 5: *STEM characterization of dislocation core situated close to the Σ3 coherent twin boundary in the material state GL-2. (a) Overview LAADF-STEM image taken with the electron beam parallel to* $[1\bar{1}0]_M$ *and* $[\bar{1}10]_T$ *directions, where the subscripts M and T stand for matrix and twin, respectively. Area marked by the black rectangle X in the lower left corner of (a) is shown in detail in (b) and (c). (b) FFT filtered HAADF-STEM image of the dislocation on the* $(111)_T$ *slip plane. (c) Burgers circuit drawn in the experimental image yields the Burgers vector projection consistent with a ½<110>-type dislocation with 60° character.*

It is important to emphasize that both the Burgers circuit drawn directly in **Fig. 5c** and the Nye tensor analysis made on the two-dimensional projection of atomic columns obtained from STEM (**Figs. 6b** and **6c**) give only the projection of the Burgers vector in the plane of the foil, which is $1/4[11\bar{2}]$. The total Burgers vector is then $\mathbf{b} = 1/4[11\bar{2}] + k[\bar{1}10]$, where the multiplier k must be chosen such that the vector **b** represents the total Burgers vector compatible with the fcc lattice. The only possible values are $k = \pm 1/4$ for which **b** becomes $1/2[10\bar{1}]$ and $1/2[01\bar{1}]$, respectively. This indirect analysis thus suggests that the dislocation shown in **Fig. 5** and analyzed in **Fig. 6** is a full 1/2<110> type dislocation. The analysis further indicates that the dislocation core is nearly compact and the separation of $1/6<112>(111)_T$ Shockley partial dislocations is, at most, only about two interplanar spacings. Here we note that the experimental COS map in **Fig. 6a** may capture local lattice column distortions due to a relaxation of the displacement field at the free surfaces of the STEM foil. The Burgers circuit drawn in **Fig. 5c** as well as the Burgers vector analysis obtained from the Nye tensor maps (see **Fig. 6b** and **c**) yield a projected Burgers vector that is consistent with either $1/2[10\bar{1}]$ or $1/2[01\bar{1}]$ complete Burgers vector. Since the line direction is oriented along $[\bar{1}10]$, the dislocation has a 60° character.

Molecular statics atomistic simulations (AS) using the recently developed Lennard-Jones (LJ) pair potential for CrMnFeCoNi [27] were employed to resolve whether the dislocation in **Figs. 5b** and **c** is compact or dissociated. The $1/2[10\bar{1}]$ dislocation was inserted into the simulation cell such that displacements of all atoms conform to the anisotropic linear-elastic strain field solution obtained by Stroh [28] (see also Hirth & Lothe [29]). The resulting elastic strain field mapped by the COS and Nye tensor techniques is shown in **Figs. 6d-f**. The block was further relaxed at 0 K using conjugate gradients, while the forces on atoms were described using the pair potential in Ref. [27]. The atoms close to the boundary of the simulation cell away from the dislocation line were held fixed at their positions obtained from the long-range elastic strain field of the dislocation. Energy minimization subject to the above constraints resulted in the splitting of the dislocation into a pair of 1/6<112> Shockley partials. The corresponding COS and Nye tensor maps are shown in **Figs. 6g-i** and are obviously different from the experimental maps in **Figs. 6a-c**. This difference is especially visible in the COS map in **Fig. 6g** where the stacking fault between the Shockley partials stretches over a distance of 3.3 nm, which is inconsistent with the experimental COS map in **Fig. 6a**. The latter results suggest that the dislocation presented in **Figs. 5b** and **c**, if dissociated at all, has partials separated by less than 0.6 nm. We expect the squeezed stacking fault is due to the local stress field created by the pile-up which acts on the investigated head dislocation. It is worth noting that this is different from observations reported by Smith et al. [18], who found a distribution of separation distances 4.82±1.93 nm between 1/6<112>{111} Shockley partials. Such discrepancies may be related to particular experimental situations since the width of the stacking fault (and the

separation of the Shockley partials) depends on the strength of the pile-up which will strongly affect the local state of deformation.

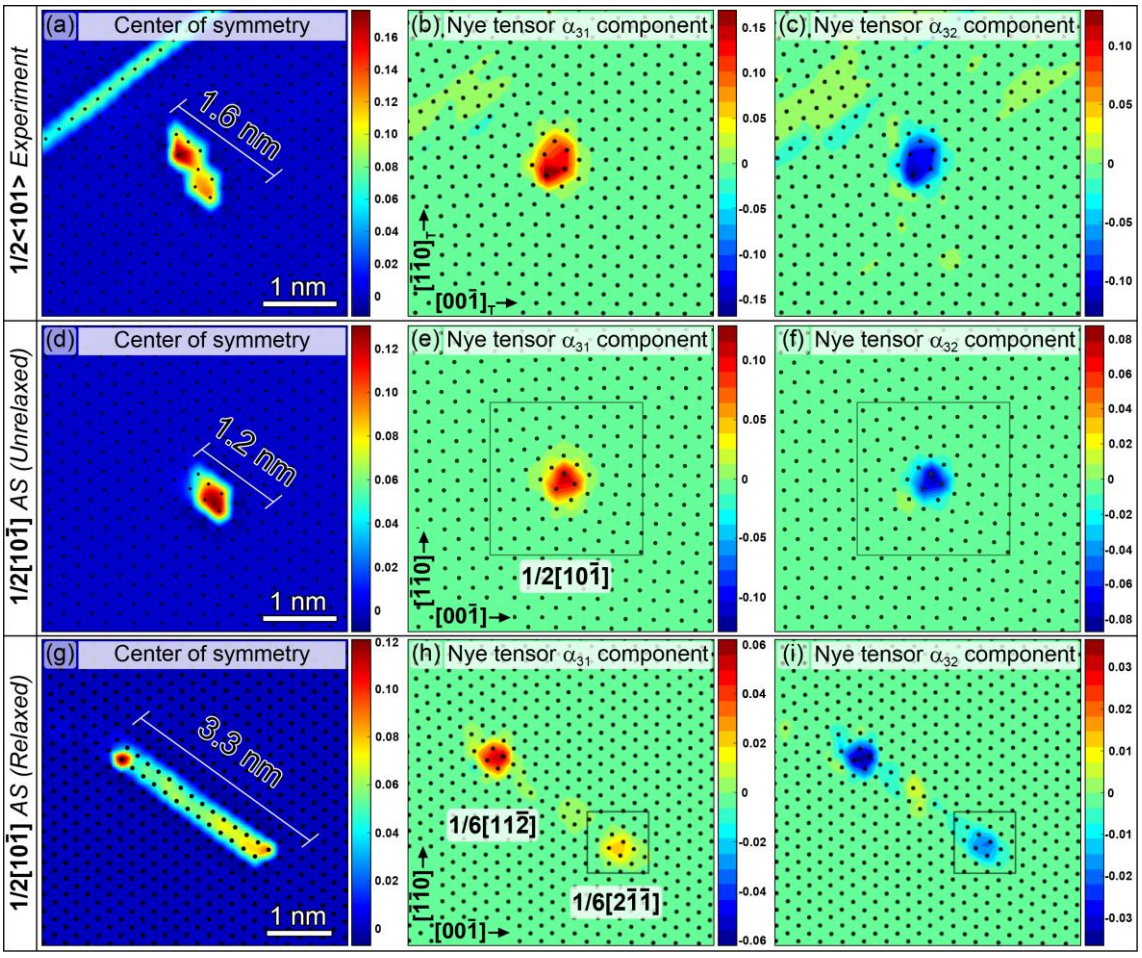

Figure 6: *(a) Local lattice distortions mapped by COS, (b)* α_{31} *and (c)* α_{32} *Nye tensor component maps based on the experimental HAADF-STEM intensities presented in* **Figs. 5b** *and* **c**. *LJ atomistic simulations of dislocation with Burgers vector* $1/2[10\bar{1}]$ *and the line parallel to* $[\bar{1}10]$ *crystallographic direction are represented by COS and Nye tensor maps: (d-f) compact dislocation, (g-i) dislocation dissociated into* $1/6[11\bar{2}]$ *and* $1/6[2\bar{1}\bar{1}]$ *Shockley partials, see text for further details.*

In order to analyze the local chemical composition and possible elemental segregation to the dislocation core region, high-spatial resolution STEM-EDS mapping was performed inside the 100×100 nm area harboring the dislocation shown in **Figs. 5b** and **c**. The corresponding HAADF image and elemental maps are presented in **Fig. 7**. This figure clearly demonstrates that none of the constituent elements of the equiatomic CrMnFeCoNi alloy segregates to the dislocation core or its nearby region in the material state GL-2.

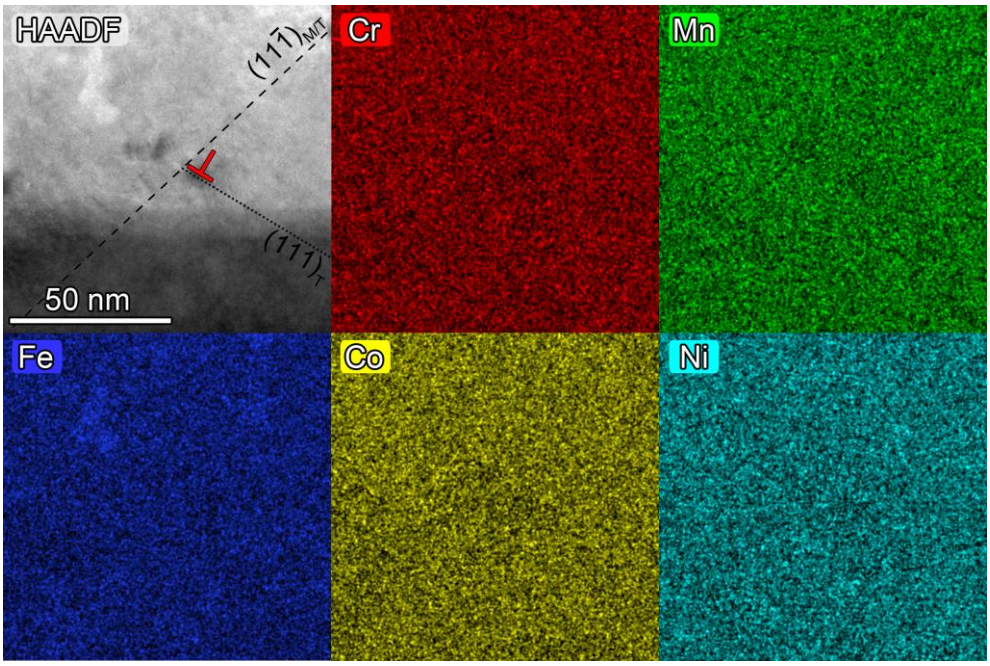

Figure 7: *STEM-EDS maps of the area harboring the dislocation shown in* **Figs. 5b** *and* **c***; material state GL-2. HAADF-STEM image of the dislocation is presented together with quantified EDS maps for Cr, Mn, Fe, Co and Ni.*

The same HAADF-STEM and STEM-EDS methodologies were used to assess dislocation cores and segregation to the core regions after the prolonged anneal at 973 K for 800 hours, material states GL-02-A and GL-2-A, see **Table 1**. Sites at which the dislocations piled-up against the Σ3 annealing twin boundaries were again targeted and analyzed. An example of one such configuration found in the material state GL-2-A is shown in **Fig. 8**. The area of interest, where a dislocation interacts with the coherent twin boundary, is marked by a black rectangle in **Fig. 8a**. We note that the selected region is located close to an intersection between the coherent twin boundary (running from the center of the image to its lower right) and a high angle grain boundary (running diagonally from lower left to upper right). Atomic resolution images of the rectangular area in **Fig. 8a** are shown in **Figs. 8b** and **c**. Noise in the HAADF-STEM image was filtered out using FFT. The white dashed rectangle in **Fig. 8b** marks the area where the analyzed dislocation is located. Similar to the case presented in **Fig. 5c**, Burgers circuit drawn in the experimental image **Fig. 8c** yields a projected Burgers vector that is consistent with either $1/2[\bar{1}01]$ or $1/2[0\bar{1}1]$ full lattice Burgers vector, see the interpretation of contrast in **Fig. 5**. As before, since the line direction is oriented along $[\bar{1}10]$, this dislocation also has 60° character.

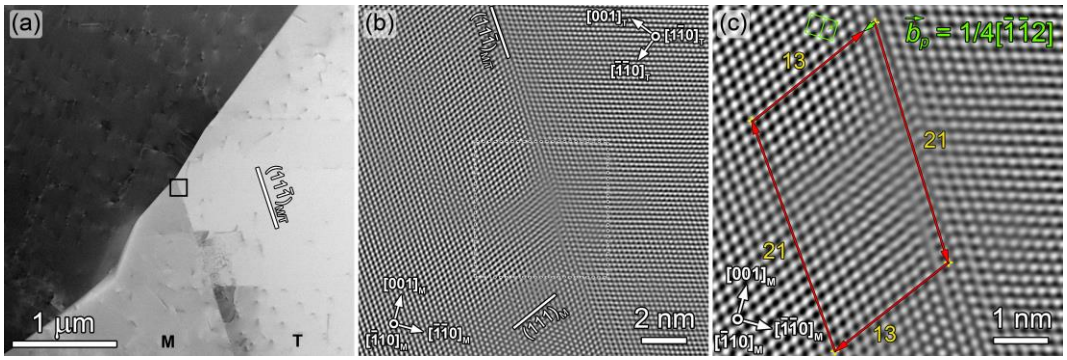

Figure 8: *STEM characterization of dislocation core situated close to the Σ3 coherent twin interface in the material state GL-2-A. (a) Overview HAADF-STEM image taken with the electron beam parallel to* $[\bar{1}10]_M$ *and* $[1\bar{1}0]_T$ *directions. Area marked by a black rectangle is shown in detail in (b) and (c). (b) FFT filtered HAADF-STEM image of the analyzed dislocation gliding on the* $(111)_M$ *slip plane. (c) Burgers circuit drawn in the experimental image yields the Burgers vector projection consistent with the* 1/2<110>*-type dislocation.*

A COS map corresponding to the area shown in **Fig. 8c** is presented in **Fig. 9a**. The map, based on the experimental HAADF-STEM intensities, highlights positions of both the twinning plane $(11\bar{1})_{M/T}$ and the smeared core of 1/2<110>$(111)_M$ dislocation. The Nye tensor calculations, using the experimental HAADF-STEM as the input, were performed to identify positions of any existing individual Shockley partials more accurately. Surprisingly, the distribution maps of α_{31} (**Fig. 9b**) and α_{32} (**Fig. 9c**) Nye tensor components clearly reveal only one dislocation core of type 1/2<110>. To further investigate whether the dislocation is dissociated, the molecular statics atomistic calculations simulated a fully relaxed displacement field of the $1/2[\bar{1}01]$ dislocation, this time considering also the presence of the nearby coherent Σ3 twin boundary. The relaxation of the atomic positions was again performed using the recently developed LJ potential for CrMnFeCoNi [27]. The resulting equilibrium atomic positions were subjected to the COS and Nye tensor analyses and the final maps are shown in **Fig. 9d** (COS map) and **Fig.9e** and **f** (maps of the Nye tensor components α_{31} and α_{32}, respectively).

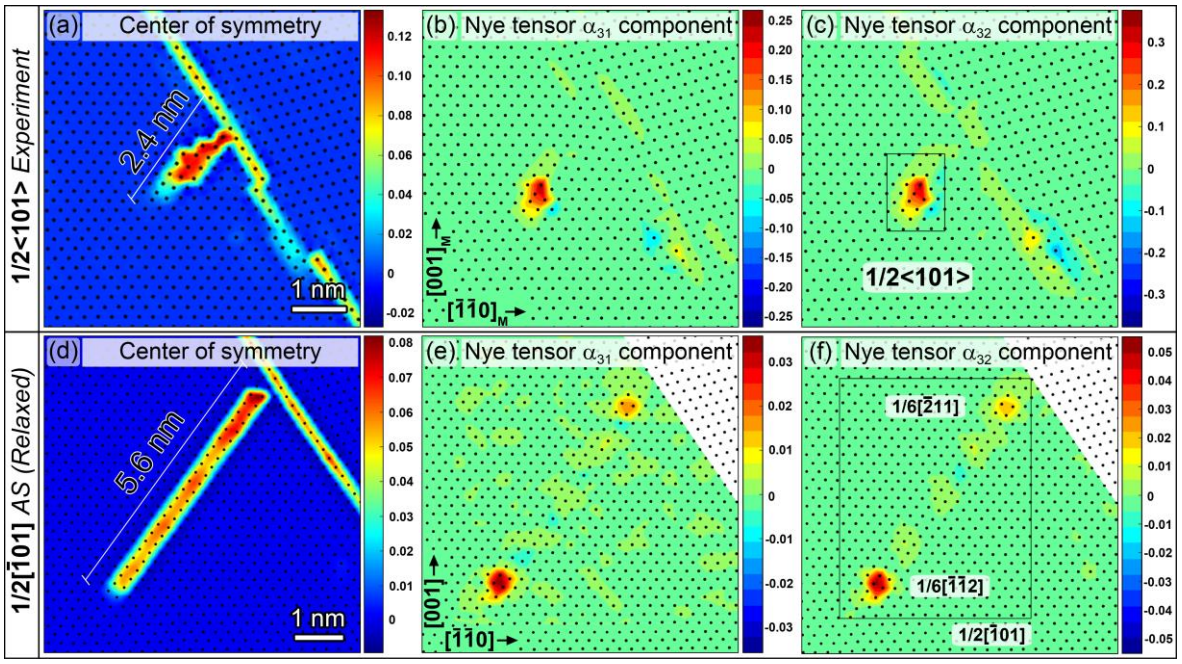

Figure 9: *(a) Local lattice distortions mapped by COS, (b) α_{31} and (c) α_{32} Nye tensor component maps based on the experimental HAADF-STEM intensities presented in* **Figs. 8b** *and* **c**. *LJ atomistic simulations of a* 1/2[$\bar{1}$01] *dislocation dissociated in the vicinity of the Σ3 coherent twin boundary: (d) the COS map and (e, f) the maps of Nye tensor components α_{31} and α_{32}, see text for further details.*

The COS map in **Fig. 9a** suggests that the core region of the dislocation observed in the experimental HAADF-STEM image (**Fig. 8c**) extends over a distance of about 2.4 nm. This is more than what was measured for the dislocation in the material state GL-2 documented in **Figs. 5b** and **c,** but less than in the simulated configuration, where the relaxed 1/2[$\bar{1}$01] dislocation is dissociated into two Shockley partials separated by about 5.6 nm, see **Fig. 9d-f**. Moreover, the simulated maps of Nye tensor components shown in **Figs. 9e** and **f** clearly reveal two Shockley partials which is not consistent with the similar maps based on the experimental image data (**Figs. 9b** and **c**). In addition, the Burgers circuit analysis indicates that the experimentally observed dislocation has a full Burgers vector of type 1/2<110>. The discrepancy between the experimental and simulated COS and Nye tensor maps is likely due to local stress fields acting on the investigated dislocations in the experimental situations that tend to squeeze the partials together and which are not considered in the simulations because of the difficulty in knowing the local stresses acting inside the material at any given point.

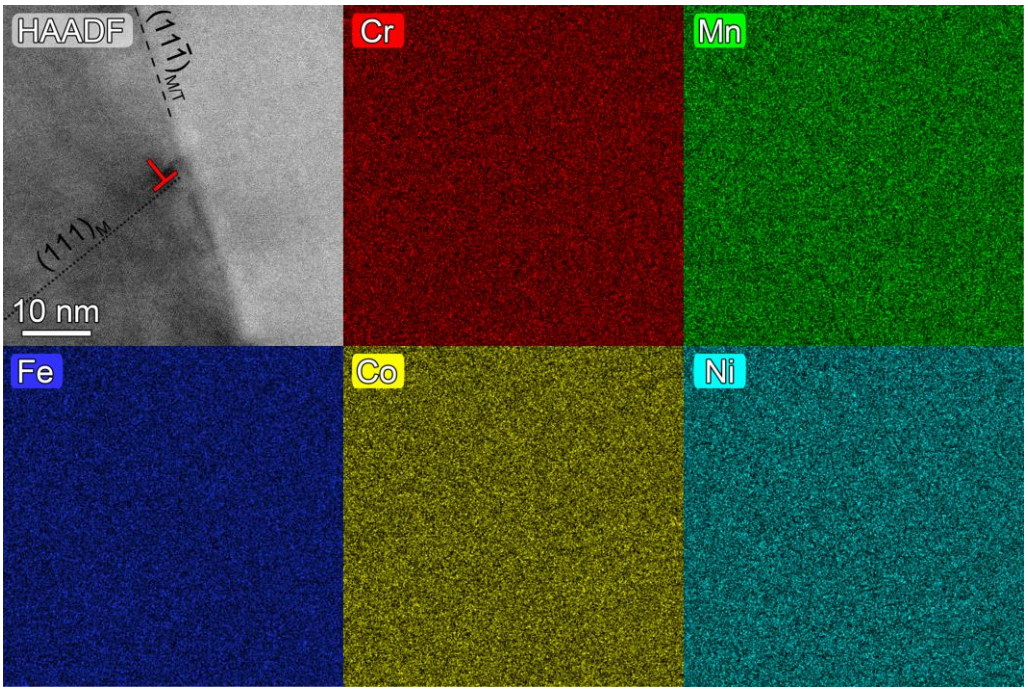

Figure 10: *STEM-EDS maps of the area harboring the dislocation shown* **Fig. 8***; material state GL-2-A. HAADF-STEM image of the dislocation is presented together with quantified EDS maps for Cr, Mn, Fe, Co and Ni.*

The chemical composition of the dislocation core and the nearby region shown in **Fig. 8** is documented in the STEM-EDS maps in **Fig. 10**. The EDS signal was collected in an area measuring 50×50 nm containing both the dislocation and the annealing twin boundary. Even after prolonged annealing at 973 K for 800 hours, the elemental maps shown in **Fig. 10** do not reveal any significant segregation to the dislocation core region. Similar results were obtained when the same high-resolution EDS elemental mapping was applied to several different sites in STEM samples taken from not only the material state GL-2-A but also from the less deformed and annealed material state GL-02-A. For completeness, we note that profiles of the chemical composition were collected along lines crossing the Σ3 annealing twin boundaries. Corresponding results are presented in the Supplementary Material as **Figs. S2** and **S3**. As can be seen, no compositional changes were detected.

3.2.3 Precipitation of sigma phase, NiMn and $M_{23}C_6$

Results of our SEM-EBSD analyses presented in **Fig. 3** confirmed previous findings that thermal exposure of the CrMnFeCoNi alloy at 973 K triggers precipitation of the Cr-rich sigma phase, see e.g. [13]. The sigma phase area fractions determined in the present study do not seem to be influenced by the mild pre-deformation preceding the annealing of the

alloy, see **Table 1**. Preferential locations for sigma phase precipitation are grain boundary triple points. One example of a Cr-rich sigma phase particle which nucleated at a triple junction in the material state GL-2-A is shown in **Fig. 11**. The corresponding STEM-EDS maps confirm that the precipitate is rich in Cr and considerably depleted in Ni (for further details, see Supplementary Material), in line with results reported by Otto et al. after long-term annealing at 973 K for 500 days [13]. It has been suggested that, while the triple point grain boundaries present thermodynamically efficient sites for nucleation, associated/surrounding grain boundaries are also important since they provide fast pathways for elemental diffusion [12].

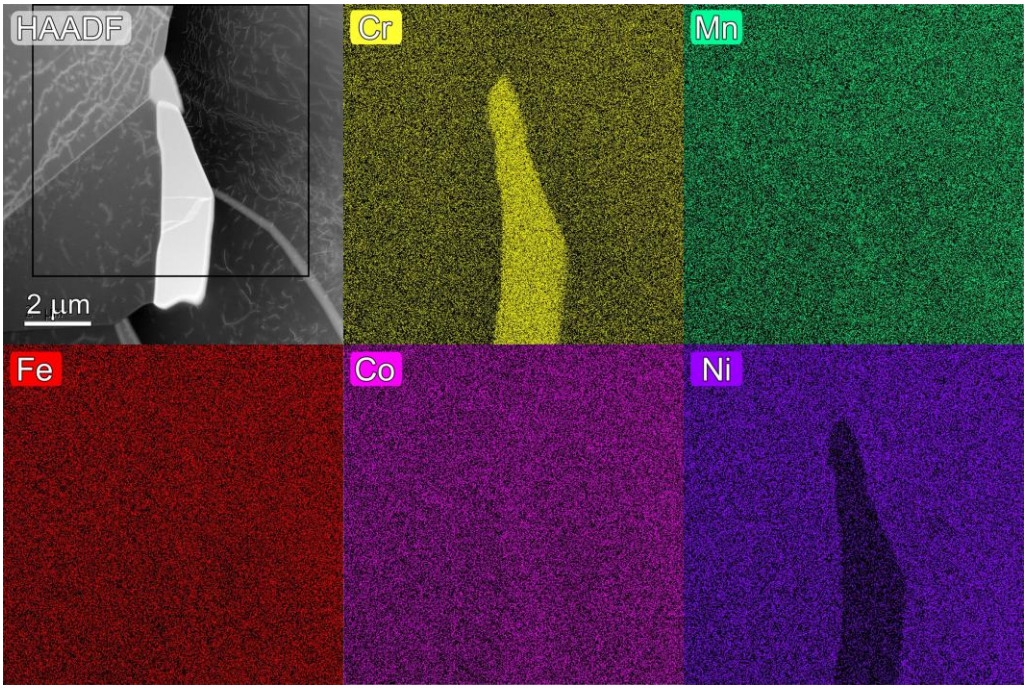

Figure 11: *STEM-EDS map of Cr-rich sigma phase nucleated at a grain boundary triple point in the material state GL-2-A. The square in the HAADF image is the area from which the EDS signal was collected. Sigma phase is rich in Cr and depleted in Ni.*

In order to check the role of the surrounding microstructure in sigma phase nucleation and growth, we measured chemical compositions in the vicinity of the particle shown in **Fig. 11**. Results of the EDS line-scan analysis are presented in **Fig. 12**. EDS analysis was performed between the two points along the arrowed line shown in **Fig. 12a**, which crosses not only the high angle grain boundary (misorientation angle of 27.7 degrees, for details see Supplementary Material) at a distance 690 nm from the particle but also several dislocations. No appreciable segregation of any element to dislocations was detected within the experimental sensitivity of the STEM-EDS technique. However, there is a clear depletion of Cr on both sides of the boundary down to 15.5 at%, accompanied by notable

enrichment in Ni (about 22.5 at.%) and also Mn (about 22 at.%). The elemental profiles shown in **Fig. 12b** suggest that the enriched/depleted region extends from the grain boundary into both adjacent grains covering about 0.8 μm on each side. The observed enrichment of Ni and Mn at the grain boundary represents a potential driving force for precipitation of the NiMn phase observed in previous studies [12,13].

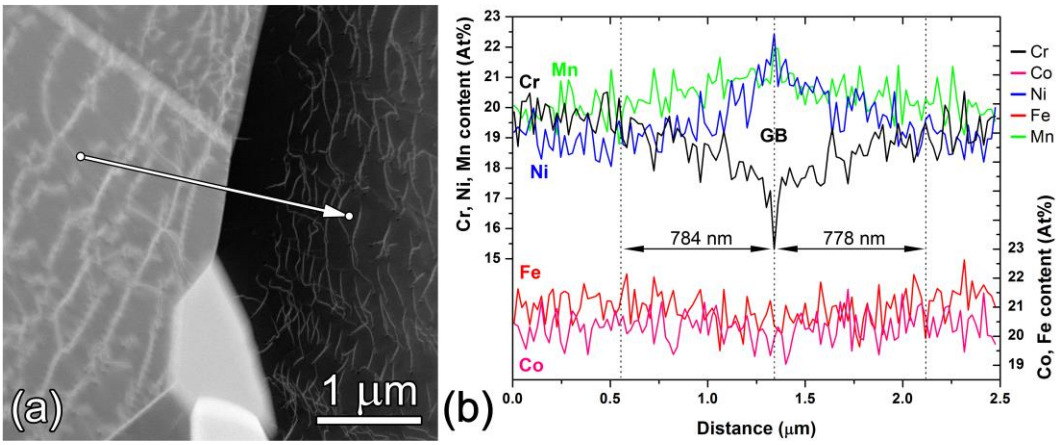

Figure 12: *(a) HAADF-STEM image of part of the area shown in* **Fig. 11**. *Elemental line-scan data were acquired across the grain boundary at a distance 690 nm from the nucleated Cr-rich sigma phase. (b) Elemental line profiles of Cr, Mn, Fe, Co and Ni.*

Earlier work by Egorushkin et al. [30] reported on the stability of the NiMn phase and set the upper temperature limit of the stability range at 938 K (i.e., it was not stable at higher than this temperature). Consistent with this prediction, recent investigations found precipitation of the tetragonal $L1_0$ NiMn phase during annealing in a temperature range 723 - 773 K [12,13]. Here we show **(Fig. 13)** that NiMn can form on grain boundaries even at 973 K, which is higher than the upper temperature limit prescribed by Egorushkin et al. A segment of the high angle grain boundary (misorientation angle of 38.8 degrees, for details see Supplementary Material) containing a large Cr-rich sigma phase particle is shown in **Fig. 13a**. A high magnification HAADF image in **Fig. 13b** reveals that this boundary segment next to the sigma phase particle is decorated by numerous NiMn precipitates with sizes of 10-20 nanometers. Related EDS chemical composition maps provide evidence that the particles are rich in Ni and Mn. The same enrichment is also proved by the EDS line-scan analysis and corresponding elemental profiles shown in **Fig. 13c** (see also the image in **Fig. 13b** for the line-scan orientation).

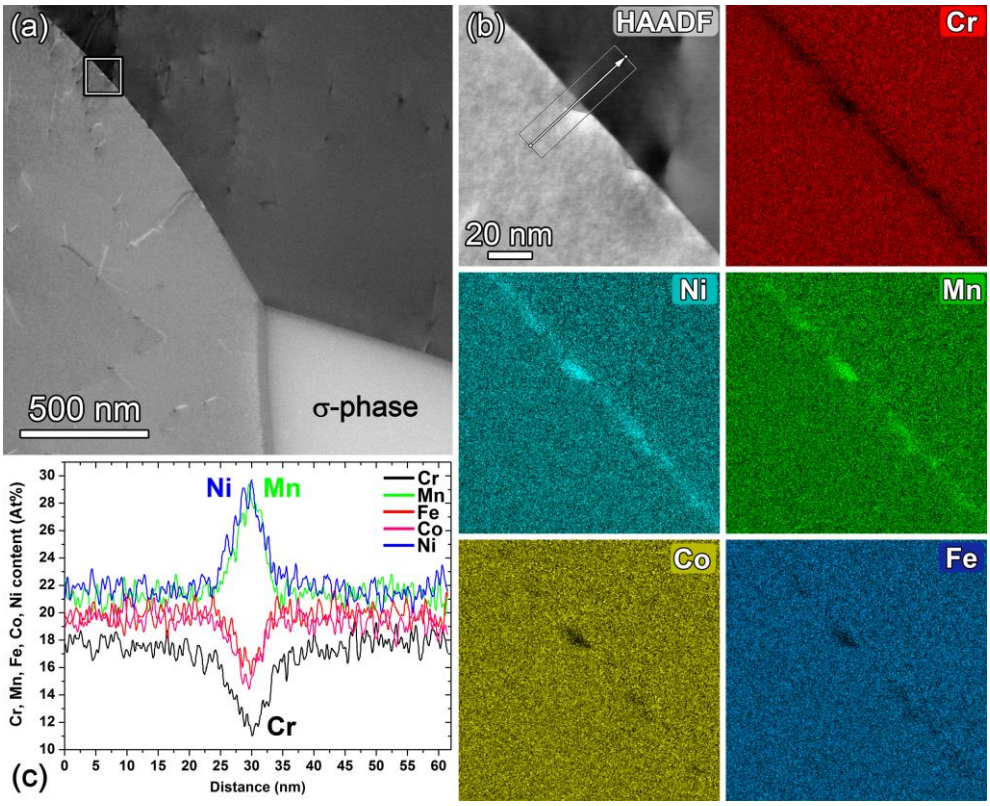

Figure 13: *NiMn precipitation on the Cr-depleted grain boundary in the vicinity of sigma phase in the material state GL-2-A. (a) Overview HAADF-STEM image with a rectangle showing the area analyzed by EDS. (b) Quantified STEM-EDS maps reveal two NiMn precipitates nucleated at the grain boundary. (c) EDS line-scan elemental profiles of Cr, Mn, Fe, Co and Ni across the NiMn precipitate.*

Recently, increasing attention has been given to carbon-doped variants of the CrMnFeCoNi alloy in which precipitation of carbides serves as a strengthening and microstructure stabilizing factor [31–33]. Interestingly, without any intentional addition of carbon to the alloy in the present study, we have nevertheless detected precipitation of Cr-rich carbides on grain boundaries in the material state GL-2-A (the carbon likely originated in the raw materials). An example is shown in **Fig. 14.** HAADF-STEM image in **Fig. 14a** displays the corresponding part of the microstructure. A schematic sketch in **Fig. 14b** provides information on the misorientations across boundaries between the grains G1, G2 and G3 involved in the precipitation process. The structure is visualized using the electron beam parallel with $[\bar{1}10]_{G1}$ zone axis in grain G1. The Cr-rich carbide is elongated with a length of approx. 2.6 μm and thickness varying from about 50 to 130 nm (with wedge shaped protrusions). It precipitated at a high angle grain boundary of grain G1 with larger part located at the G1/G3 grain boundary segment (misorientation angle of 24.2 degrees, for details see Supplementary Material) and smaller part at the G1/G2 segment.

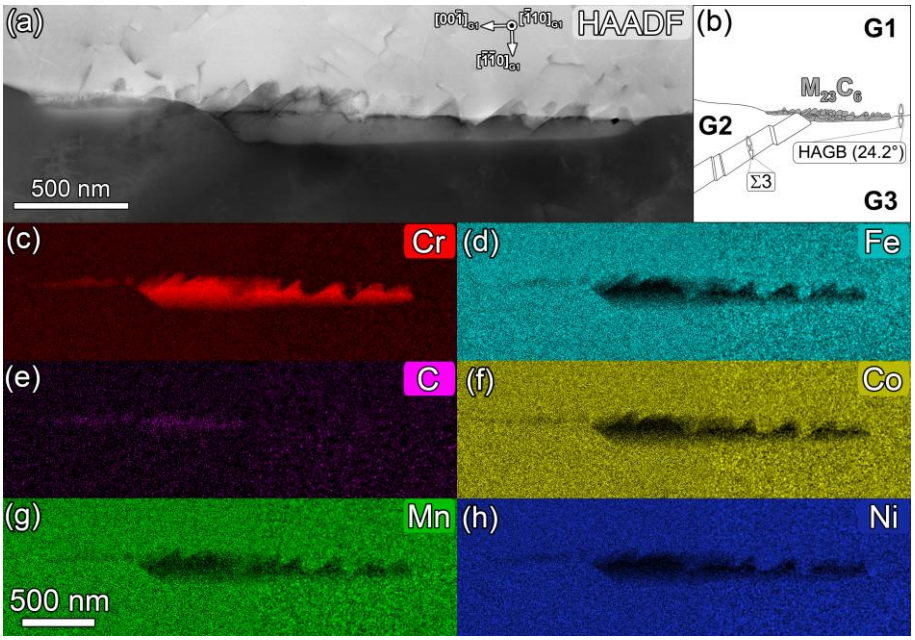

Figure 14: *Three grains G1, G2 and G3 in the material state GL-2-A are involved in the precipitation of the elongated Cr-rich carbide consisting of many small nano-carbides. (a) HAADF-STEM image taken with the electron beam parallel to* $[\bar{1}10]_{G1}$ *zone axis of grain G1. (b) Schematic sketch presenting mutual misorientations between the grains and location of the Cr-rich carbides. (c-h) Quantified STEM-EDS elemental maps prove that the particles are rich in Cr and C, and depleted in Mn, Fe, Co and Ni.*

High-spatial resolution STEM-EDS as well as atomic resolution HAADF-STEM data were collected and analyzed in order to identify the carbide phase unambiguously and exclude the Cr-rich sigma phase which exhibits a similar morphology. Corresponding quantified STEM-EDS elemental maps are shown in **Fig. 14(c-h).** The higher magnification HAADF image in **Fig. 14a** reveals that the elongated particle consists of an array of several small precipitates. The corresponding elemental maps show that these particles are rich in Cr and C and depleted in Mn, Fe, Co and Ni. These results are further confirmed by the EDS line-scan chemical analysis presented in **Figs. 15a** and **15b**. More details about the detection of carbon in EDS spectra and differences between the Cr-rich sigma phase and the Cr-rich $M_{23}C_6$ carbide are reported in Supplementary Material, **Figs. S5**, **S6** and **S7**. The atomic structure of the carbide particle was investigated in the small rectangular area marked by X in **Fig. 15a**. The atomic resolution HAADF-STEM image in **Fig. 15c** was acquired with the incident electron beam parallel to the $[\bar{1}10]$ zone axis. In **Fig. 15d**, the experimentally obtained and FFT filtered atomic structure image was compared to a $Cr_{23}C_6$ model created in the Crystal Maker software using parameters of Bowman et al. [34]. In the model, carbon atoms are colored black and chromium atoms pink. Finally, the experimentally obtained

FFT diffraction pattern in **Fig. 15e** is compared to the selected area electron diffraction (SAD) pattern of $Cr_{23}C_6$ simulated using Crystal Maker software and shown in **Fig. 15f**. The FFT diffraction patterns acquired in the matrix grain G1 and the $M_{23}C_6$ precipitate confirm a cube-on-cube orientation relationship. The corresponding SAD patterns clearly show that the lattice parameter of $M_{23}C_6$ is approximately three times larger than the lattice parameter of the FCC CrMnFeCoNi matrix (lattice parameter a = 0.360 nm [35]). Small lattice misfit between the carbide and FCC matrix is in agreement with experimentally observed semi-coherent interface populated with misfit dislocations.

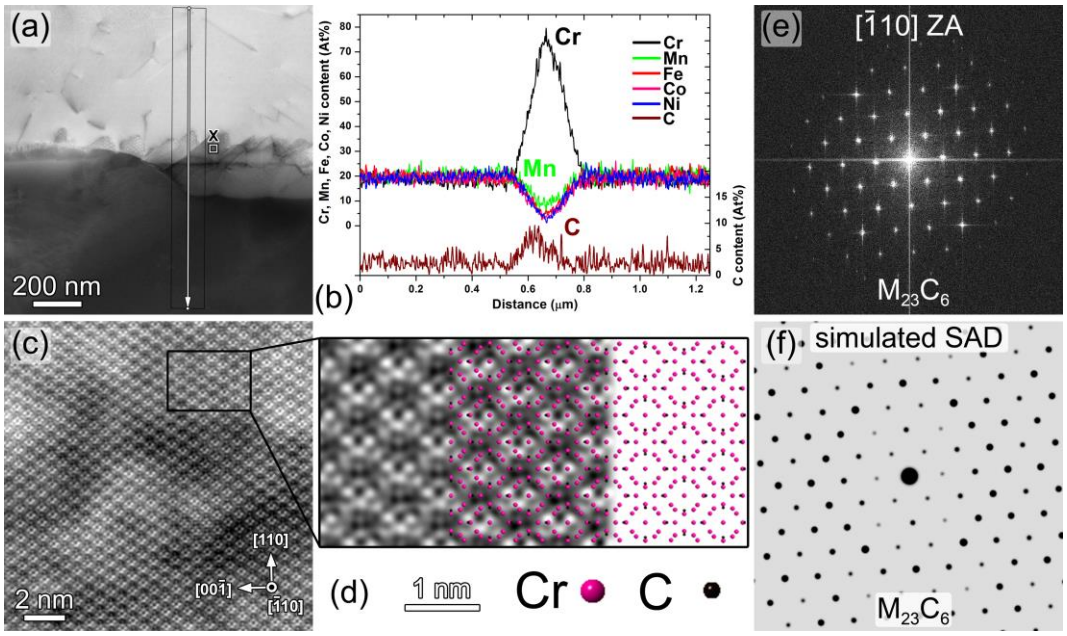

Figure 15: *Detailed chemical and atomic structure analysis of Cr-rich $M_{23}C_6$ carbides presented in* **Fig. 14**. *(a) Overview HAADF-STEM image shows the position of the EDS line scan (white arrow) and the small rectangle X highlights the area probed with atomic resolution. (b) Corresponding EDS line-scan elemental profiles. (c) FFT filtered HAADF-STEM image of carbide atomic structure viewed along* [1̄10] *zone axis. (d) FFT filtered experimental image of the carbide atomic structure is compared to the model constructed using the Crystal Maker software. Experimentally obtained FFT diffraction pattern (e) is compared to the SAD pattern of $Cr_{23}C_6$ (f) simulated by the Crystal Maker software.*

4. DISCUSSION

The present study focuses on the thermodynamic stability of the equiatomic CrMnFeCoNi FCC solid solution, in particular whether the alloy elements segregate to dislocations. To collect relevant experimental data, we first deformed the CrMnFeCoNi samples in tension

at RT to small plastic strains and subsequently annealed them at 973 K for 800 hours. Two stress-strain curves shown in **Fig. 1** demonstrate excellent reproducibility of our tensile experiments. Both curves exhibit a shallow stress minimum right after yield at plastic strain 0.2%. This stress minimum may be due to glide plane softening resulting from the passage of pioneering dislocations. In such a scenario, the leading dislocations of a pile-up destroy atomic bonds in a region that may exhibit some degree of short range ordering [36,37]. The leading dislocations thus randomize the material along their slip planes which provides an energetically favorable path for the following dislocations generated by the same dislocation source [7]. Such a mechanism, along with the extended planar cores of dissociated dislocations [18], may rationalize the planar slip generally observed in the early deformation stage of the CrMnFeCoNi alloy, see e.g. **Fig. 4** and [7]. Alternatively, the shallow minimum may correspond to yielding of grain boundaries that become fully transparent for dislocations only after an accumulation of some plastic strain inside grains [17]. Considering the grain size d and the yield strength σ_{02} listed in **Table 1**, our ($d^{-1/2}$, σ_{02}) data point is consistent with the Hall-Petch plot reported by Otto et al. [7].

The plastic tensile strain of the order of 2% at RT increased the dislocation density up to 9.4×10^{13} m^{-2} and formed a sufficient number of dislocation segments oriented along the <110>-type crystallographic directions. These specific dislocation orientations resulted from interactions of dislocation pile-ups on {111}-type crystallographic planes with special Σ3 boundaries, as originally suggested by Smith [18], or with {311}-type boundaries, see **Fig. 4**. The exact orientation of dislocation segments parallel to the <110> directions is of utmost importance for a credible analysis of dislocation cores using electron beams aligned with the same <110> direction in the HR-STEM sample, see **Figs. 5** and **8**. According to the quantitative TEM results summarized in **Table 1**, the dislocation density slightly decreased to 7.2×10^{13} m^{-2} after prolonged annealing at 973 K for 800 hours. Although some degree of dislocation density decrease due to annealing is to be expected, we note that the dislocation density difference between the material states GL-2 and GL-2-A is within the experimental error of Ham's technique. Most importantly, the grain and crystallite size data listed in **Table 1** clearly show that the prolonged annealing at 973 K for 800 hours did not cause any appreciable grain growth or recrystallization. This conclusion holds for all the investigated material states irrespective of whether or not the alloy had been subjected to pre-deformation prior to annealing. Furthermore, even after the prolonged anneal, many dislocations remained in contact with the special grain boundaries and kept their <110> orientation required for the HR-STEM analysis, as is documented in **Fig. 8**.

The detailed analyses presented in **Figs. 5, 6, 8** and **9** show that the 1/2<110> dislocations interacting with the Σ3 boundaries are either compact or very narrowly dissociated into two partials. The departure from the centro-symmetric configuration around the 60°

dislocations, rendered by the COS analysis in **Fig. 6a**, may involve a contribution from relaxation at the free surfaces of the thin STEM foil. Further work is required to determine the extent to which these surface relaxations contribute to the COS maps. In our experimental methodology, we consider situations like in **Fig. 4**, where a leading dislocation of a pile-up is pushed against a special boundary such that it aligns parallel to the <101> type crystallographic direction. In the tensile experiment, the pushing force on the leading dislocation is due to a superposition of the applied stress and stress fields of trailing dislocations in the slip plane [17]. Even though some stress relaxation and related pile-up redistribution may occur upon unloading after the tensile experiment, we expect that internal stresses continue to act on the leading dislocations even after unloading, see e.g. dislocation pile-up highlighted by an arrow in **Fig. 6** in the study by Otto and co-workers [7]. These internal stresses represent another factor which may control the width of stacking fault ribbons, that is, the splitting distances between Shockley partial dislocations. Another factor is the variations in local chemical arrangement along the stacking fault plane which could influence the local stacking fault energy as investigated in detail by Smith et al. [18]. Results of the present study cannot distinguish between these factors and additional experiments and discrete dislocation dynamics simulations are needed to disentangle the individual contributions.

Surprisingly, high spatial resolution EDS experiments performed in the present study using the Super-X detector did not reveal any elemental segregation to individual dislocations even after prolonged annealing at 973 K for 800 hours, see results presented in **Figs. 7** and **10**. Within the sensitivity of the Super-X EDS mapping, there was no concentration gradient detected which would confirm e.g. an enrichment of dislocation cores by chromium. This cannot be fully reconciled with results reported by Zhou et al. who observed precipitation of Cr-rich particles on dislocation cell walls in heavily cold-rolled and partially recovered CrMnFeCoNi alloy [14]. However, when comparing the observations of Zhou et al. with the high spatial resolution EDS results of the present study, two distinctions must be taken into account. First, the dislocation densities in their heavily cold-rolled and partially recovered alloy were likely higher by at least two orders of magnitude than the value 9.4×10^{13} m^{-2} measured in the present study after 2% plastic tensile strain. Unfortunately, Zhou et al. did not provide any quantitative estimate of their dislocation density [14]. Second, after the partial recovery at 873 K, the Cr-rich precipitates were found just at dense planar arrangements of dislocations (dislocation cell walls [14]), a microstructural feature which is absent in the material states investigated in the present study. Therefore, based on the results of our Super-X EDS mapping of the *individual* dislocation cores after prolonged annealing at 973 K, it can be concluded that elastic interactions between the stress fields of *isolated individual* dislocations and the elemental constituents of the CrMnFeCoNi alloy are not sufficient to drive any detectable segregation

to dislocations. This conclusion is noteworthy given that the dislocation cores investigated in this study were situated close to special boundaries, the locations of which might provide additional thermodynamic forces for nucleation and growth of the Cr-rich precipitates. The results of high spatial resolution EDS experiments reported in this study cast some doubts on the interpretation of the 923 K creep data in terms of segregation and dragging of Cr atmospheres by individual dislocations, as has been suggested without any microstructural evidence, by Kang and co-workers [15]. Since no Cr segregation to individual dislocations was observed in the present study after annealing at 973 K for 800 hours, it is highly unlikely that any such segregation would take place during a creep experiment performed at 923 K and lasting only about 20 hours [15].

According to earlier studies [11–13,35], temperatures around 973 K provide the best conditions for the precipitation of the Cr-rich tetragonal sigma phase. For the equiatomic CrMnFoCoNi alloy, these earlier results were confirmed by the annealing experiments performed in this study, see **Fig. 3**. The sigma phase area fractions evaluated from the SEM micrographs and summarized in **Table 1** show that the increment of dislocation density due to the 2% tensile pre-strain does not influence the sigma phase precipitation during the subsequent annealing at 973 K. This is another indication that a claimed segregation to, and diffusion of chromium along, dislocation cores [15] should not cause any measurable effects at 973 K and 800 hours. Our results presented in **Figs. 12** and **13** may shed more light on the kinetics of the sigma phase precipitation and associated diffusion of Cr. The Super-X EDS line-scan reveals Cr-denuded zones which extend to distances of about 800 nm from the grain boundary. Therefore, we suggest that the transport of Cr towards the matrix-particle interface likely proceeds in two steps. First, Cr is transported by bulk diffusion over short distances towards the grain boundary and then, by faster grain boundary diffusion, towards a grain boundary triple-point where the sigma phase nucleates and grows. This transport of chromium towards a growing sigma phase particle in turn enhances concentrations of Ni and Mn and results in a precipitation of nano-sized NiMn particles on the grain boundary, see **Fig. 13**. Therefore, the succession of precipitate reactions in equiatomic CrMnFeCoNi after prolonged annealing at 973 K for 800 hours can be summarized as (i) precipitation of Cr-rich sigma phase predominantly at grain boundary triple junctions followed by (ii) precipitation of NiMn particles on the Cr-depleted grain boundary segments. This sequence is fully in line with the qualitative TTT diagram originally proposed by Otto et al. [13] which assumes a temperature regime where the simultaneous occurrence of Cr-rich sigma phase and NiMn phase is possible. Our results also do not contradict a quantitative TTT diagram recently published by Chou and co-workers [38] since their experimental data span short times. Apparently, at longer annealing times, such as those of the present study, the TTT curves of the Cr-rich sigma phase and NiMn phase must intersect to allow for simultaneous precipitations. In passing we note that

the precipitation of the NiMn particles observed in the present study after annealing at 973 K does not support results reported by Egorushkin et al. who claimed the NiMn phase is stable only below 938 K [30]. Finally, when the chemical driving force (supersaturation) for formation of Cr-rich sigma phase is increased in the off-equiatomic alloy $Cr_{26}Mn_{20}Fe_{20}Co_{20}Ni_{14}$, sigma phase can nucleate and grow at progressively less favorable sites, including grain boundaries (away from triple points), twin boundaries, and grain interiors, and at faster rates compared to the equiatomic alloy [39].

Besides the Cr-rich sigma phase situated at the grain boundary triple junctions and NiMn precipitates on the Cr-depleted grain boundaries, we also observed Cr-rich $M_{23}C_6$ carbides, see **Figs. 14** and **15**. We presume these carbides resulted from the trace levels of carbon present in the raw materials used for alloy production. Nucleation and growth of $M_{23}C_6$ carbides have been broadly investigated in austenitic steels [40]. It is known that, at high temperatures, these carbides nucleate very quickly and can be found even in stabilized steels after very short aging times, e.g. less than one hour at 973 K [40]. Their preferential nucleation sites are grain boundaries, but they can be found also inside grains, at twin boundaries and dislocations or stacking faults. According to the literature [34], structure of the $M_{23}C_6$ phase is cubic (space group 225, Pearson symbol cF116, with a lattice parameter between 1.057 and 1.068 nm depending on the chemical content of the alloy). Interestingly, the carbides shown in **Figs. 14** and **15** exhibit different nucleation site and morphology as compared to the Cr-rich $M_{23}C_6$ precipitates in Sanicro 25 (Fe-25Ni-22.5Cr alloy) after exposure at 973 K [41]. In the present study, the Cr-rich $M_{23}C_6$ carbides were found at a grain boundary triple junction, similar to the Cr-rich sigma phase precipitates. On the other hand, the atomic structure and the lattice parameters of the Cr-rich $M_{23}C_6$ carbides characterized here by advanced electron microscopy techniques, is similar to that reported for Sanicro 25 [41]. Our results thus indicate a potential for strengthening the CrMnFeCoNi alloys by the carbide phases [31,32].

5. SUMMARY AND CONCLUSIONS

The equiatomic CrMnFeCoNi alloy was cold-rolled and annealed at 1173 K for 1 hour. This thermo-mechanical treatment yielded a fully recrystallized single-phase FCC microstructure with an average grain size of 19 μm and a low dislocation density (~ 10^{12} m^{-2}). The dislocation density increased to 9.4×10^{13} m^{-2} after a pre-deformation at room temperature to a tensile plastic strain of 2.3%. The pre-deformed samples were subsequently annealed at 973 K for 800 hours to investigate the influence of low plastic strains on the thermodynamic stability of the alloy. Particular emphasis was given to whether any of the elemental constituents of the alloy segregated to individual dislocations.

Six material states were investigated using state-of-the-art electron microscopy techniques. Based on this experimental effort, following conclusions can be drawn:

1) The tensile stress-strain curves of the starting microstructural state showed excellent reproducibility and exhibited a shallow stress minimum right after plastic yielding. This early stress minimum can be attributed to either a softening of glide planes, when dislocations at the head of pile-ups disrupt partial short range order, or a gradual transmission of slip through grain boundaries as discussed by Schneider [17].

2) The tensile pre-deformation activated planar slip of 1/2<110>-type dislocations on {111}-type glide planes. Interactions of the planar slip with special Σ3 and general {311}-type grain boundaries formed a number of dislocation segments with <110> crystallographic orientation suitable for a credible end-on analysis of dislocation cores in HR-STEM.

3) Annealing at 973 K for 800 hours did not cause any appreciable grain growth or recrystallization irrespective of whether or not the alloy had been subjected to tensile pre-deformation prior to the annealing. The dislocation density decreased only slightly to 7.2×10^{13} m^{-2} after the prolonged anneal leaving a sufficient number of <110>-oriented dislocation segments for the HR-STEM analysis.

4) Cores of 1/2<110> dislocations pushed against the Σ3 grain boundaries are close to the compact configuration. The width of stacking fault ribbons depends on (*i*) the sum of the pushing force due to dislocation-dislocation interactions and the superposed applied stress and/or (*ii*) the local chemical arrangements along the stacking fault plane and the related variations in the local stacking fault energy [18]. Results of the present study do not allow us to distinguish between these two factors and additional experiments and numerical simulations are required to resolve this complex issue.

5) Within the sensitivity of the Super-X EDS mapping, there was no concentration gradient detected which would confirm an enrichment of dislocation cores by any elemental constituent of the alloy after the annealing at 973 K for 800 hours. Under these conditions, the elastic interactions between the stress fields of *isolated individual* dislocations and the elemental constituents of the CrMnFeCoNi alloy are not sufficient to drive any detectable segregation to dislocations.

6) Tetragonal Cr-rich sigma phase precipitates formed at grain boundary triple points in both undeformed and mildly pre-deformed specimens after annealing at 973 K for 800 hours. The enhancement of dislocation density from $\sim 10^{12}$ m^{-2} in the undeformed

specimens to 9.4×10^{13} m^{-2} in the pre-strained specimens does not accelerate the nucleation and growth of the sigma phase precipitates.

7) Formation of sigma phase was accompanied by a depletion of Cr and concomitant enrichment of Ni and Mn in a narrow zone near the grain boundaries. The latter factor contributed to the precipitation of NiMn particles at grain boundaries after prolonged annealing.
8) The precipitation of the NiMn particles observed in the present study after annealing at 973 K contradicts a previous prediction that the NiMn phase is not stable above 938 K [30].

9) Cr-rich $M_{23}C_6$ carbides precipitate at grain boundary triple junctions similar to the Cr-rich sigma phase.

ACKNOWLEDGEMENTS

VM, RG, TZ and AD acknowledge financial support from the CSF under the contract no. 14-22834S. Electron microscopy investigations were partly performed using facilities of the CEITEC Nano Research Infrastructure (ID LM2015041, MEYS CR, 2016-2019). Additional financial support has been provided by the Ministry of Education, Youth and Sports of the Czech Republic under the project CEITEC 2020 (LQ1601) and by the IPM ASCR Brno through the project IPMinfra no. LM 2015069. EPG is supported by the U.S. Department of Energy, Office of Science, Basic Energy Sciences, Materials Sciences and Engineering Division. MJM and MH acknowledge financial support from the National Science Foundation under the contract No. #DMR-1905748. Support is also acknowledged from the Thermo Fisher Scientific & Czechoslovak Microscopy Society fellowship awarded to Milan Heczko. Authors would like to thank Jiri Tobias for his help with the mechanical testing of material and Dagmar Herzanova for preparation of twin-jet electropolished disc foils.

REFERENCES

[1] R.C. Reed, The Superalloys: Fundamentals and Applications, Cambridge University Press, Cambridge, 2006. https://doi.org/10.1017/CBO9780511541285.
[2] T. Fujita, Current Progress in Advanced High Cr Ferritic Steels for High-temperature Applications., ISIJ International. 32 (1992) 175–181. https://doi.org/10.2355/isijinternational.32.175.

[3] A.B. Parsa, P. Wollgramm, H. Buck, C. Somsen, A. Kostka, I. Povstugar, P.-P. Choi, D. Raabe, A. Dlouhy, J. Müller, E. Spiecker, K. Demtroder, J. Schreuer, K. Neuking, G. Eggeler, Advanced Scale Bridging Microstructure Analysis of Single Crystal Ni-Base Superalloys, Advanced Engineering Materials. 17 (2015) 216–230. https://doi.org/10.1002/adem.201400136.
[4] A. Aghajani, C. Somsen, G. Eggeler, On the effect of long-term creep on the microstructure of a 12% chromium tempered martensite ferritic steel, Acta Materialia. 57 (2009) 5093–5106. https://doi.org/10.1016/j.actamat.2009.07.010.
[5] B. Cantor, I.T.H. Chang, P. Knight, A.J.B. Vincent, Microstructural development in equiatomic multicomponent alloys, Materials Science and Engineering: A. 375–377 (2004) 213–218. https://doi.org/10.1016/j.msea.2003.10.257.
[6] A. Gali, E.P. George, Tensile properties of high- and medium-entropy alloys, Intermetallics. 39 (2013) 74–78. https://doi.org/10.1016/j.intermet.2013.03.018.
[7] F. Otto, A. Dlouhý, C. Somsen, H. Bei, G. Eggeler, E.P. George, The influences of temperature and microstructure on the tensile properties of a CoCrFeMnNi high-entropy alloy, Acta Materialia. 61 (2013) 5743–5755. https://doi.org/10.1016/j.actamat.2013.06.018.
[8] Z. Wu, H. Bei, G.M. Pharr, E.P. George, Temperature dependence of the mechanical properties of equiatomic solid solution alloys with face-centered cubic crystal structures, Acta Materialia. 81 (2014) 428–441. https://doi.org/10.1016/j.actamat.2014.08.026.
[9] V. Yardley, I. Povstugar, P.-P. Choi, D. Raabe, A.B. Parsa, A. Kostka, C. Somsen, A. Dlouhy, K. Neuking, E.P. George, G. Eggeler, On Local Phase Equilibria and the Appearance of Nanoparticles in the Microstructure of Single-Crystal Ni-Base Superalloys, Advanced Engineering Materials. 18 (2016) 1556–1567. https://doi.org/10.1002/adem.201600237.
[10] J.-W. Yeh, S.-K. Chen, S.-J. Lin, J.-Y. Gan, T.-S. Chin, T.-T. Shun, C.-H. Tsau, S.-Y. Chang, Nanostructured High-Entropy Alloys with Multiple Principal Elements: Novel Alloy Design Concepts and Outcomes, Advanced Engineering Materials. 6 (2004) 299–303. https://doi.org/10.1002/adem.200300567.
[11] E.J. Pickering, R. Muñoz-Moreno, H.J. Stone, N.G. Jones, Precipitation in the equiatomic high-entropy alloy CrMnFeCoNi, Scripta Materialia. 113 (2016) 106–109. https://doi.org/10.1016/j.scriptamat.2015.10.025.
[12] B. Schuh, F. Mendez-Martin, B. Völker, E.P. George, H. Clemens, R. Pippan, A. Hohenwarter, Mechanical properties, microstructure and thermal stability of a nanocrystalline CoCrFeMnNi high-entropy alloy after severe plastic deformation, Acta Materialia. 96 (2015) 258–268. https://doi.org/10.1016/j.actamat.2015.06.025.
[13] F. Otto, A. Dlouhý, K.G. Pradeep, M. Kuběnová, D. Raabe, G. Eggeler, E.P. George, Decomposition of the single-phase high-entropy alloy CrMnFeCoNi after prolonged

anneals at intermediate temperatures, Acta Materialia. 112 (2016) 40–52. https://doi.org/10.1016/j.actamat.2016.04.005.
[14] W. Zhou, L.M. Fu, P. Liu, X.D. Xu, B. Chen, G.Z. Zhu, X.D. Wang, A.D. Shan, M.W. Chen, Deformation stimulated precipitation of a single-phase CoCrFeMnNi high entropy alloy, Intermetallics. 85 (2017) 90–97. https://doi.org/10.1016/j.intermet.2017.02.010.
[15] Y.B. Kang, S.H. Shim, K.H. Lee, S.I. Hong, Dislocation creep behavior of CoCrFeMnNi high entropy alloy at intermediate temperatures, Materials Research Letters. 6 (2018) 689–695. https://doi.org/10.1080/21663831.2018.1543731.
[16] A.H. Chokshi, High temperature deformation in fine grained high entropy alloys, Materials Chemistry and Physics. 210 (2018) 152–161. https://doi.org/10.1016/j.matchemphys.2017.07.079.
[17] M. Schneider, E.P. George, T.J. Manescau, T. Záležák, J. Hunfeld, A. Dlouhý, G. Eggeler, G. Laplanche, Analysis of strengthening due to grain boundaries and annealing twin boundaries in the CrCoNi medium-entropy alloy, International Journal of Plasticity. 124 (2020) 155–169. https://doi.org/10.1016/j.ijplas.2019.08.009.
[18] T.M. Smith, M.S. Hooshmand, B.D. Esser, F. Otto, D.W. McComb, E.P. George, M. Ghazisaeidi, M.J. Mills, Atomic-scale characterization and modeling of 60° dislocations in a high-entropy alloy, Acta Materialia. 110 (2016) 352–363. https://doi.org/10.1016/j.actamat.2016.03.045.
[19] P.B. Hirsch, A. Howie, R.B. Nicholson, D.W. Pashley, M.J. Whelan, L. Marton, Electron Microscopy of Thin Crystals, Physics Today. 19 (1966) 93–95. https://doi.org/10.1063/1.3047787.
[20] A. Dlouhý, J. Pešička, Estimate of foil thickness by stereomicroscopy technique, Czechoslovak Journal of Physics. 40 (1990) 539–555. https://doi.org/10.1007/BF01599778.
[21] A. Dlouhý, G. Eggeler, Superdislocation line directions in gamma prime-particles after double shear creep superalloy single crystals, Practical Metallography. 33 (1996) 629–642.
[22] L. Agudo Jácome, G. Eggeler, A. Dlouhý, Advanced scanning transmission stereo electron microscopy of structural and functional engineering materials, Ultramicroscopy. 122 (2012) 48–59. https://doi.org/10.1016/j.ultramic.2012.06.017.
[23] R.K. Ham, The determination of dislocation densities in thin films, Philosophical Magazine. 6 (1961) 1183–1184. https://doi.org/10.1080/14786436108239679.
[24] C. Hartley, Y. Mishin, Characterization and visualization of the lattice misfit associated with dislocation cores, Acta Materialia. 53 (2005) 1313–1321. https://doi.org/10.1016/j.actamat.2004.11.027.

[25] V.A. Vorontsov, L. Kovarik, M.J. Mills, C.M.F. Rae, High-resolution electron microscopy of dislocation ribbons in a CMSX-4 superalloy single crystal, Acta Materialia. 60 (2012) 4866–4878. https://doi.org/10.1016/j.actamat.2012.05.014.
[26] H.L. Yakel, Atom distributions in sigma phases. I. Fe and Cr atom distributions in a binary sigma phase equilibrated at 1063, 1013 and 923 K, Acta Crystallographica Section B Structural Science. 39 (1983) 20–28. https://doi.org/10.1107/S0108768183001974.
[27] R. Gröger, V. Vitek, A. Dlouhy, Effective pair potential for random fcc CoCrFeMnNi alloys, Modelling and Simulation in Materials Science and Engineering. (2020). https://doi.org/10.1088/1361-651X/ab7f8b.
[28] A.N. Stroh, Steady State Problems in Anisotropic Elasticity, Journal of Mathematics and Physics. 41 (1962) 77–103. https://doi.org/10.1002/sapm196241177.
[29] J.P. Hirth, J. Lothe, Theory of dislocations, 2. ed., reprint, Krieger Publishing Company, Malabar, Fla, 1992.
[30] V.E. Egorushkin, S.N. Kulkov, S.E. Kulkova, Electronic structure and the theory of phase transformations in NiMn, Physica B+C. 123 (1983) 61–68. https://doi.org/10.1016/0378-4363(83)90011-6.
[31] J. Peng, Z. Li, L. Fu, X. Ji, Z. Pang, A. Shan, Carbide precipitation strengthening in fine-grained carbon-doped FeCoCrNiMn high entropy alloy, Journal of Alloys and Compounds. 803 (2019) 491–498. https://doi.org/10.1016/j.jallcom.2019.06.204.
[32] W. Lu, C.H. Liebscher, F. Yan, X. Fang, L. Li, J. Li, W. Guo, G. Dehm, D. Raabe, Z. Li, Interfacial nanophases stabilize nanotwins in high-entropy alloys, Acta Materialia. 185 (2020) 218–232. https://doi.org/10.1016/j.actamat.2019.12.010.
[33] N. Gao, D.H. Lu, Y.Y. Zhao, X.W. Liu, G.H. Liu, Y. Wu, G. Liu, Z.T. Fan, Z.P. Lu, E.P. George, Strengthening of a CrMnFeCoNi high-entropy alloy by carbide precipitation, Journal of Alloys and Compounds. 792 (2019) 1028–1035. https://doi.org/10.1016/j.jallcom.2019.04.121.
[34] A.L. Bowman, G.P. Arnold, E.K. Storms, N.G. Nereson, The crystal structure of Cr23C6, Acta Crystallographica Section B Structural Crystallography and Crystal Chemistry. 28 (1972) 3102–3103. https://doi.org/10.1107/S0567740872007526.
[35] G. Laplanche, P. Gadaud, O. Horst, F. Otto, G. Eggeler, E.P. George, Temperature dependencies of the elastic moduli and thermal expansion coefficient of an equiatomic, single-phase CoCrFeMnNi high-entropy alloy, Journal of Alloys and Compounds. 623 (2015) 348–353. https://doi.org/10.1016/j.jallcom.2014.11.061.
[36] J. Olfe, H. Neuhäuser, Dislocation groups, multipoles, and friction stresses in α-CuZn alloys, Physica Status Solidi (a). 109 (1988) 149–160. https://doi.org/10.1002/pssa.2211090115.
[37] E.P. George, D. Raabe, R.O. Ritchie, High-entropy alloys, Nature Reviews Materials. 4 (2019) 515–534. https://doi.org/10.1038/s41578-019-0121-4.

[38] T.H. Chou, J.C. Huang, C.H. Yang, S.K. Lin, T.G. Nieh, Consideration of kinetics on intermetallics formation in solid-solution high entropy alloys, Acta Materialia. 195 (2020) 71–80. https://doi.org/10.1016/j.actamat.2020.05.015.
[39] G. Laplanche, S. Berglund, C. Reinhart, A. Kostka, F. Fox, E.P. George, Phase stability and kinetics of σ-phase precipitation in CrMnFeCoNi high-entropy alloys, Acta Materialia. 161 (2018) 338–351. https://doi.org/10.1016/j.actamat.2018.09.040.
[40] T. Sourmail, Precipitation in creep resistant austenitic stainless steels, Materials Science and Technology. 17 (2001) 1–14. https://doi.org/10.1179/026708301101508972.
[41] V. Mazánová, M. Heczko, J. Polák, Fatigue crack initiation and growth in 43Fe-25Ni-22.5Cr austenitic steel at a temperature of 700 °C, International Journal of Fatigue. 114 (2018) 11–21. https://doi.org/10.1016/j.ijfatigue.2018.04.033.